Bulk RNA-seq and scRNA-seq analysis reveal an activation of immune response and compromise of secretory function in major salivary glands of obese mice

Heping Huang [1], Ce Gao *,[1], Shuai Wang [1], Fen Wu, Jinsong Wei, Jinrong Peng *

MOE Key Laboratory for Molecular Animal Nutrition, College of Animal Sciences, Zhejiang University, Hangzhou 310058, China

ARTICLE INFO

ABSTRACT

Obesity affects the function of multiple organs/tissues including the exocrine organ salivary glands. However, the effects of obesity on transcriptomes and cell compositions in the salivary glands have yet been studied by bulk RNA-sequencing and single-cell RNA-sequencing. Besides, the cell types in the sublingual gland, one of the three major salivary glands, have yet been characterized by the approach of single-cell RNA-sequencing. In this report, we find that the histological structure of the three major salivary glands are not obviously affected in the obese mice. Bulk RNA-sequencing analysis shows that the most prominent changes observed in the three major salivary glands of the obese mice are the mobilization of transcriptomes related to the immune response and down-regulation of genes related to the secretory function of the salivary glands. Based on single-cell RNA-sequencing analysis, we identify and annotate 17 cell clusters in the sublingual gland for the first time, and find that obesity alters the relative compositions of immune cells and secretory cells in the major glands of obese mice. Integrative analysis of the bulk RNA-sequencing and single-cell RNA-sequencing data confirms the activation of immune response genes and compromise of secretory function in the three major salivary glands of obese mice. Consequently, the secretion of extracellular matrix proteins is significantly reduced in the three major salivary glands of obese mice. These results provide new molecular insights into understanding the effect of obesity on salivary glands.

1. Introduction

In mammals, the mouth is surrounded by numerous minor glands and three major salivary glands (SGs), namely submandibular gland (SMG), sublingual gland (SLG) and parotid gland (PG). As an exocrine system, the function of SGs is to produce the saliva to water and lubricate the mouth, aid in digestion and protect the teeth and oral cavity. Some factors, such as Sjögren's Syndrome (SS) (a chronic autoimmune disease) [1,2] or radiation therapy for treating head and neck cancer patients [1,2], are known to affect the function of SGs regarding saliva secretion and contents [3]. The outcome is the reduction in saliva secretion and alteration in the saliva contents which will affect the oral function and health, including food intaking and taste, periodontitis and oral infections etc. PG and SLG are mainly composed of serous and mucous acini,

respectively, whereas SMG, the largest gland in murine, is composed of both serous and mucous acini [4,5]. Classic histological and recent single-cell RNA-sequencing (scRNA-seq) analysis have identified main cell types in SMG and PG, including serous acinar cells, mucous acinar cells, seromucous cells, intercalated ductal cells, striated ductal cells, excretory ductal cells, granular convoluted tubules (GCT) and circulating blood and immune cells [1,4–10]. However, the cell types in SLG have yet been characterized by the approach of scRNA-seq.

Obesity, characterized by increased fat deposition in the body, can be caused not only by genetic factors but also environmental factors such as high energy diet and life style [11,12]. Obesity is associated with many chronic diseases and the prevalence of obesity has become a great threat to human health and is now a world-wide concern. Obesity inevitably affects the function of multiple organs/tissues including the SGs. Reports have shown that obese individuals were diagnosed of reduction in saliva secretion, alterations in the saliva composition and increase in oxidative damage, which have been hypothesized to cause dental caries

and periodontal disease [13–17], however, the cellular and molecular bases for these symptoms remain elusive. High-fat diet (HFD) induced obese mice (DIO mice) have widely been used as a model to study the consequence of obesity. In DIO mice, SMG showed changes in the expression of long non-coding RNAs (lncRNAs) and messenger RNAs (mRNAs) by a microarray analysis [18]. However, the effects of obesity on gene expression profiles and cell compositions in three major SGs have yet been studied by bulk RNA-sequencing (RNA-seq) and scRNA-seq.

In this study, we analyzed the transcriptomes in the three major SGs by bulk RNA-seq and cell compositions in SMG, SLG and PG by scRNA-seq in both normal and DIO mice. This study has two aims: 1) to identify genes whose expression in three major SGs is affected in DIO mice, and 2) to find out whether the ratios of different cell types are affected in the SMG, SLG and PG in the DIO mice. Detailed gene ontology (GO) analysis of the bulk RNA-seq data allowed us to conclude that DIO mice mobilized transcriptomes related to the immune response and down-regulated the genes related to the secretory pathways in coping with obesity. Meanwhile, we identified and annotated 17 cell types in SLG through the scRNA-seq approach. Consistent with the bulk RNA-seq analysis, we found that the ratios of immune cells within three major SGs were significantly increased in the DIO mice. The implications of our findings in understanding the effect of obesity on the SGs of obese patients are discussed.

2. Material and methods

2.1. Animal model

To exclude the effect of periodic change of estrogen and progesterone levels on the female physiology and gene expression, C57BL/6J male mice were used in this study. All animal procedures were performed in full accordance with the Guide for the Care and Use of Laboratory Animals and were approved by the Animal Ethics Committee in Zhejiang University (approved application number: 11871). Mice were housed in a temperature-controlled environment under a 12 hr light:dark cycle with free access to water and food. C57BL/6J male mice were fed ad libitum with either chow diet containing 20.5 % protein, 4 % fat and 5 % fiber (SLACAM company, Shanghai) (NC mice) or high-fat diet containing 26 % protein, 35 % fat and 26 % carbohydrate (Research Diets, 35 % fat) started at week 5 postnatal (DIO mice). Weight was weighed at the time point as stated in the text.

2.2. Blood glucose content measurement

For glucose- and insulin-tolerance tests, over-night-fasted mice (for glucose tolerance test) or 6hr-fasted mice (for insulin tolerance test) were injected intraperitoneally with glucose (2 g per kg body weight) or insulin (0.75 U per kg body weight), respectively. Blood glucose levels were measured at 0, 15, 30, 60, 90 and 120 min after glucose or insulin administration. The content of blood glucose in the glucose or insulin tolerance test was measured through tail vein bleeding with the use of the Accu-Chek Active Blood Glucose Meter (Roche, Germany).

2.3. Oil red O staining, hematoxylin-eosin (H&E) staining and Alcian blue staining

Oil red O staining, hematoxylin-eosin (H&E) staining and Alcian blue staining were performed by HaokeBio (Hangzhou,China). For Oil red O staining, the liver tissue was dissected from NC and DIO mice, respectively, and was fixed with 4 % PFA (paraformaldehyde) and sectioned for Oil red O staining (Sigma-Aldrich, USA),

counter-stained with hematoxylin. For H&E or Alcian blue staining, SMG, SLG and PG were separately dissected from NC and DIO mice and were fixed with 4 % PFA and sectioned for H&E and Alcian blue staining, respectively. The latter was counter-stained with nuclear fast-red staining. Stained samples were visualized and photographed under a microscopic scanner (KF-PRO-120).

2.4. Quantitative analysis of Oil red O or Alcian blue staining

The signals of Oil red O or Alcian blue staining were quantitatively analyzed by Image-Pro Plus 6.0 software (Media Cybernetics, USA). Three non-overlapping fields were randomly selected for each section under a 20-fold objective lens, and images were collected. The pixels of the Oil red O or the Alcian blue staining signal were the cumulative values of the area of interest and the total pixels of all colors in the same area were also collected. The relative Oil red O or Alcian blue staining signal intensity was expressed as the ratio of red (for Oil red O) or blue (for Alcian blue) pixels versus total pixels.

2.5. RNA-seq samples and data analysis

SMG, SLG and PG from the same individual mice were dissected and combined together as one sample for total RNA extraction. RNA purification, library construction and cDNA sequencing were performed by poly-T oligo-attached magnetic beads, random hexamer primer and M−MuLV Reverse Transcriptase, DNA Polymerase I and RNase H, AMPure XP system (Beckman Coulter,Beverly, USA). RNA samples were analyzed by the Agilent Bioanalyzer 2100 system. The clustering of the index-coded samples was performed on a cBot Cluster Generation System using TruSeq PE Cluster Kit v3-cBot-HS (Illumia) according to the manufacturer's instructions. After cluster generation, the library preparations were sequenced on an Illumina Novaseq platform and 150 bp paired-end reads were generated. The sequencing data were deposited in National Genomics Data Center, China National Center for Bioinformation (CNCB-NGDC), Genome Sequence Archive (GSA, https://ngdc.cncb.ac.cn/gsa/) (submission ID: subCRA011670; BioProject ID: PRJCA010884). Clean reads were mapped to the mouse genome (GRCm39) using the software Hisat2 v2.0.5 with default parameters [19]. The raw counts generated by the software featureCounts v1.5.0-p3 were concatenated together and submitted to DEseq2 to obtain normalized expression levels [20]. The threshold parameters for differentially expressed genes (DEGs) were an absolute $\log_2$ fold change ≥ 1 and corrected p-value < 0.05. Unsupervised hierarchical clustering analysis was performed using the pheatmap package (version 1.0.8, https://cran.r-project.org/web/packages/pheatmap/index.html) and Gene Ontology (GO) analysis using the KOBAS-i (version 3.0) software tool [21].

2.6. Quantitative PCR

Total RNA was extracted from mouse SGs using TRIpureReagent (Aidlab, RN0102) according to the manufacturer's instructions. Total RNA was treated with DNaseI (Thermo Scientific, EN0521) prior to reverse transcription. Synthesis of cDNA was performed using 1 μg total RNA from each sample using M−MLV Reverse Transcriptase (Invitrogen, 28025–021). qPCR was performed on a CFX96 Real-Time System (Bio-Rad,C1000ThermalCycler) with AceQq PCR SYBR Green Master Mix (Vazyme, Q111-02) according to the manufacturer's instructions and analyzed on a Bio-Rad CFX96 apparatus (Bio-Rad). Primer sequences are listed in Supplementary Table S1.

2.7. Stimulated saliva collection, saliva flow rate and peroxidase activity assay

For stimulation of saliva secretion, anesthetized mice after intraperitoneal injection with anesthetic consisting of ketamine (25 μ g per gram of body weight) and xylazine (1.1 μg per gram of body weight) were injected with 100 μg/mL pilocarpine hydrochloride (HY-B0726, MCE, America) (0.5 μ g per gram of body weight). Cotton wool was plugged into the mouth of mice to absorb the saliva and stimulated saliva were collected by a pipette from the mouth. Collected saliva was used immediately. Saliva flow rate was estimated by the volume of saliva collected within 30 min. 30 μl of saliva was used for the peroxidase activity assay using the Micro Peroxidase (POD) Assay kit (BC0095, Solarbio, Beijing) according to the manufacturer's instruction.

2.8. Protein analysis and immunohistochemical staining

Antibodies against CD4 (ER1706-80, HuaBio, Hangzhou), CD8A (0108–7, HuaBio, Hangzhou), CD79A (EM1902-29, HuaBio, Hangzhou), MUC13 (ER1913-37, HuaBio, Hangzhou), MUC20 (A15968, ABclonal,Wuhan), α-Amylase (3796,Cell Signaling Technology, America) andβ-Actin (AC026, ABclonal, Wuhan) were purchased. For western blot analysis, total protein was extracted from the salivary glands by RIPA buffer (P0013B, Beyotime) and the protein concentration was determined with Bradford Protein Assay Kit (P0006C, Beyotime). 30 μg of protein sample was separated by SDS PAGE (10 %) followed by transferring to polyvinylidene difluoride membranes. Following blocking with 5 % nonfat milk at room temperature for 1 h, the membranes containing significant proteins were incubated with primary antibodies at 4℃ overnight. Subsequently, the membranes were incubated with a HRP-conjugated antibody (HA1001, HA1006, HuaBio, Hangzhou) for 1.5 h at room temperature. Target proteins were detected with an enhanced chemiluminescence kit (E411-04, Vazyme, Nanjing) and the staining signals were acquired with a ChemiScope 3400 (Clinx Science Instruments, Shanghai). Western blot was performed as previously described [22].

For immunohistochemical staining, the expression of target proteins was detected by the correspondent antibodies. In brief, paraffin sections were treated with 3 % H_2O_2 to block endogenous peroxidase activity. Sodium citrate heat induced (about 120℃) antigen retrieval was used for all specimens. The sections were washed three times with PBS plus 0.1 % Tween for 10 min each. The sections were blocked by 3 % bovine serum albumin followed by overnight incubation at 4℃ with primary antibodies and incubation at room temperature for 1 h with biotinylated secondary antibodies. Immunopositive reactions were visualized using 3,3′ diaminobenzidine tetrahydrochloride solution. Sections were counterstained with hematoxylin at room temperature for 1 min. Images were captured using a microscopic scanner (KF-PRO-120).

2.9. scRNA-seq and data analysis

The microwell-seq approach [23] was adopted for scRNA-seq in this study. SMG, SLG and PG samples were separately dissected and digested with 1 mg/mL collagenase typeⅡ(A004174,Sangon Biotech), 0.5 mg/mL dispase (A002100,Sangon Biotech) and ACCU-TASE (STEMCELL Technologies) (SMG and SLG were digested at 37 ℃ for 30 min and PG for 60 min). Single cell library was generated as described [24]. High-throughput DNA sequencing was performed on Illumina HiSeq X Ten PE150 platform. Aligned reads and gene-barcode matrices were then generated from FASTQ files including Read 1 and Read 2 using dropEst (v0.8.5). Data analysis was performed with R package Seurat (v4.0). Elbow plot was used to determine the optimal principal components (PCs) for cluster-

ing. Data filtering and analysis for each SGs was as the following: for SLG, nFeature_RNA (unique genes) between 100 and 2500, percent.mt (mitochondrial gene percentage) < 20, dimensions 1:30, resolution 0.5; for SMG, nFeature_RNA between 120 and 2500, percent.mt < 20, dimensions 1:30, resolution 0.5; for PG, nFeature_RNA between 100 and 2500, percent.mt < 10, dimensions 1:20, resolution 0.5. The sequencing data were deposited together with the bulk RNA-seq data in the CNCB-NGDC, Genome Sequence Archive (GSA, https://ngdc.cncb.ac.cn/gsa/) (submission ID: sub-CRA011670; BioProject ID: PRJCA010884).

The CIBERSORTx tool [25] was used as a deconvolution approach to validate the compositions of cell types in SLG in the NC mouse with a published SLG RNA-seq data [26]. The CellChat package [27] was adopted to analyze the cell–cell interaction in the SMG, SLG and PG, respectively, with the purpose to compare the cell–cell interaction difference between the NC and DIO mice. The CIBERSORTx and CellChat analysis were performed according to the method instruction by using the default parameters, respectively.

2.10. Statistics and reproducibility

Unless stated otherwise, all parameters were tested using unpaired two-tailed Student's *t*-test. Significant *p*-value in all statistical analyses was obtained using GraphPad Prism 8 (GraphPad Software). A *p*-value below 0.05 was considered statistically significant. Unless stated otherwise, the experiments were not randomized and investigators were not blinded to allocation during experiments. Comparison of cell compositions between NC and DIO mice was performed using the scCODA method [28].

3. Results

3.1. Histological structure of SGs in DIO mice appeared to be relatively normal

C57BL/6J male mice were divided into two groups (four mice each), with one group fed always with normal chow diet (NC mice) while another with HFD (DIO mice) for 30 weeks starting at week-5 postnatal (Fig. 1A, top panel). HFD induced significant weight gains to DIO mice from week-13 postnatal onwards (Fig. 1A, lower panel). At week-35 postnatal, all four DIO mice (DIO-1 to DIO-4) exhibited an obvious obese phenotype (Fig. 1B, left panel), weighed 51.2 g (g) in average while the four NC mice (NC-1 to NC-4) weighed 33.1 g in average (Fig. 1B, right panel). At week-30 postnatal, this batch of NC and DIO mice was subjected to glucose tolerance test by intraperitoneal injection of glucose (2 g/kg of the body weight) after overnight-fasting. The result showed that the blood glucose content reached to the peak 30 min (min) after injection and then began to decrease in both the NC and DIO mice (Fig. 1C). However, after reaching peak, the blood glucose content decreased much faster in the NC mice than in the DIO mice within the duration of examination (120 min after injection) (Fig. 1C). At week-31 postnatal, these mice were tested for insulin tolerance by intraperitoneal injection of insulin (0.75U/kg of the body weight) after 6 h (hrs) fasting. The blood glucose contents in both NC and DIO mice dropped to a low point 60 min after insulin injection and was then gradually recovered (Fig. 1D). We noticed that, despite containing a higher level of blood glucose, the DIO mice displayed a similar reduction rate of blood glucose content as did the NC mice after insulin injection, however, the recovery rate, though not statistically significant, appeared to be slower in DIO mice compared with NC mice (Fig. 1D, Supplementary Fig. S1). These results suggest that the DIO mice retained a relatively normal insulin response although they appeared to display hyper-
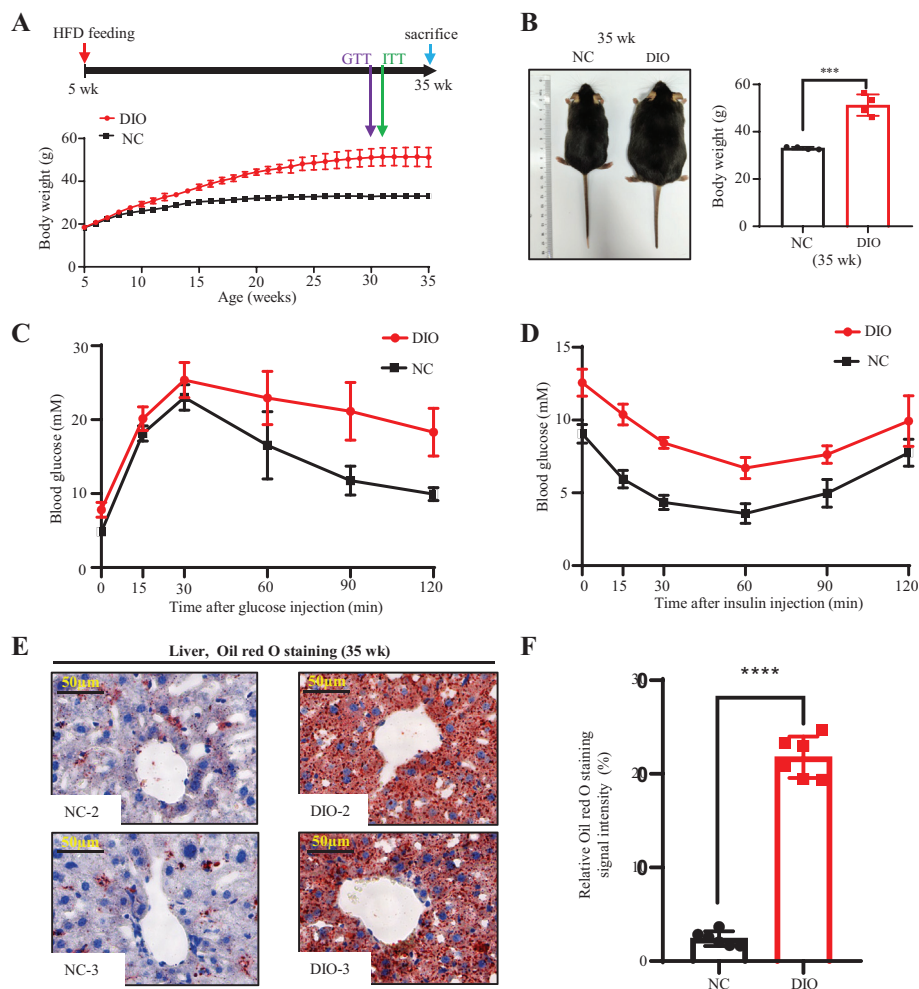
Fig. 1. Evaluation of the DIO mouse model. (A) Top panel: Diagram showing the feeding strategy and the time point for injection of glucose (GTT) (purple arrow, 30 wk) or insulin (ITT, 31 wk) (green arrow). Lower panel: Growth curve of mice fed with normal chow diet (NC) (black curve) and HFD (red curve) (DIO) starting at week 5 postnatal for 30 weeks. Significant difference ($p < 0.001$) was seen starting from week 13 postnatal. Data are mean ± s.e.m. (B) Left: A photo showing a NC mouse and a DIO mouse. Right: Statistics showing the significant difference in weight between NC and DIO mice (n = 4) at 35 wk. (C-D) Blood glucose level in NC and DIO mice (n = 4) at different time points after the injection of glucose (C) (2 g/kg of body weight) or insulin (0.75U/kg of body weight) (D). (E-F) Images showing the Oil red O staining (E) and histogram showing the quantification of the staining signal (ratio of the red color pixels against total color pixels) based on 3 liver sections from each NC (NC-2 and NC-3) and DIO (DIO-2 and DIO-3) mice (F). Statistical significance was determined using unpaired two-tailed Student's *t*-test. ***, $p < 0.001$, ****, $p < 0.0001$.

glycemia. The hyperglycemia symptom is possibly due to the chronic effect of HFD feeding on the liver function [29,30] since Oil red O staining showed that DIO-2 and DIO-3 mice conferred a fatty liver phenotype when compared with NC-2 and NC-3 mice at week-35 postnatal (Fig. 1E-F).

Next, we went to examine whether HFD induced obesity would lead to any alterations to the SGs morphology. We dissected SMG and SLG from two NC (NC-2 and NC-3) and two DIO (DIO-2 and DIO-3) mice and PG from other two NC (NC-7 and NC-8) and two DIO (DIO-7 and DIO-8) mice, respectively, at week-35 postnatal. Hematoxylin-eosin (H&E) staining did not reveal obvious changes in the characteristic histological structures of acini and ducts in SMG, SLG and PG between NC and DIO mice although it appeared that there was less mucous excretion in three SGs in the DIO mice (Fig. 2A-C). These results suggest that HFD feeding does not affect the gross development of the three major SGs.

3.2. Identification of DEGs between NC and DIO mice by bulk RNA-seq

The SMG, SLG and PG dissected from the same mouse were combined as one SG sample for total RNA extraction. Total six SG samples, including three NC mice (NC-1, −2 and −3) and three DIO mice (DIO-1, −2, and −3) at week-35 postnatal from the above

batch (Fig. 1B), were used in the RNA-seq analysis for comparing the SG transcriptomes between NC and DIO mice. Number of clean bases from the six SG RNA-seq samples were all exceeded 5.8 GB, and data filtering based on the Clean Q30 Bases Rate program revealed that the Q30 for all six samples was more than 92.8 % (Supplementary Table S2), demonstrating that the reads obtained were of high quality. Next, we aligned the clean sequences to the mouse genome (GRCm39 database, webpage: https://www.ncbi. nlm.nih.gov/assembly/GCF_000001635.27) and found that at least 97 % of total clean reads had a corresponding match in the mouse genome for each SG sample (Supplementary Table S2). 19422, 20,188 and 19,907 genes in three NC mice, and 19545, 19,394 and 19,525 genes in three DIO mice were detected (Supplementary Table S2; accession number in database: GSA: PRJCA010884), respectively. The expression levels of genes in each sample were calculated based on the TPM (transcripts per million) method [31].

Hierarchical clustering of all mapped genes from six SG samples showed that the three NC mice represented a clad while the three DIO mice represented another (Supplementary Fig. S2A). Further data analysis using DESeq2 [20] identified 543 upregulated DEGs and 212 downregulated DEGs (TPM > 1 in at least one replicate, | $\log_2$ fold-change| ≥ 1, *p-adjust* < 0.05) in the DIO-mice (Supplementary Fig. S2B, Tables S3-S5). To evaluate the quality of the data, we
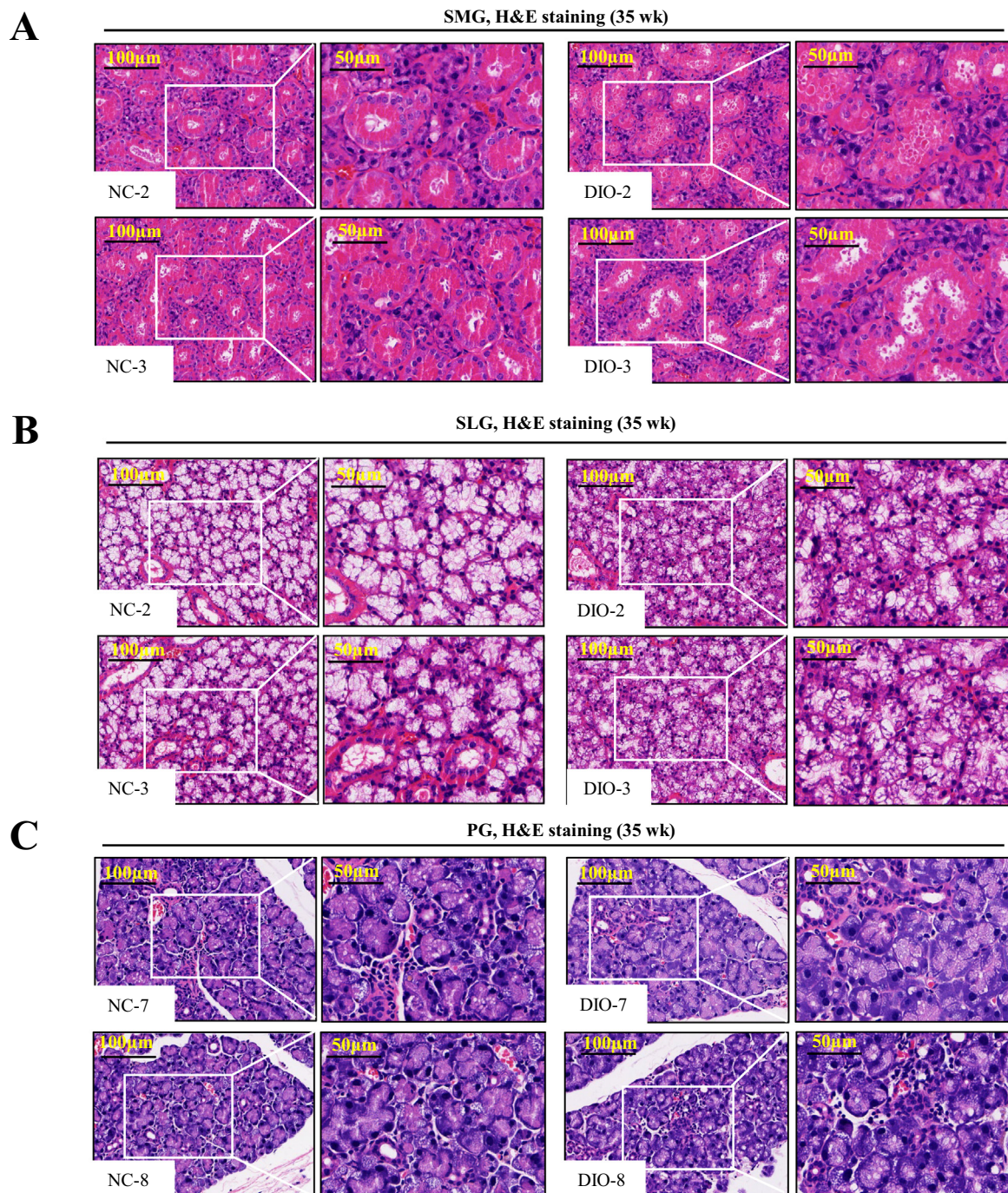
Fig. 2. Morphologies of the SGs in DIO mice are relatively normal. (A-C) H&E staining of sections of the SMG (A) and SLG (B) dissected from two NC (NC-2 and -3) and two DIO (DIO-2 and -3) mice and of PG (C) from NC-7, NC-8, DIO-7 and DIO-8. An enlarged view of the area within the white frame is shown on the right.

analyzed, via qPCR, the expression of 17 genes in the three NC and three DIO mice, including 7 upregulated, 4 downregulated, and 6 no-change genes. Except one up-regulated (*Dclk1*) and one down-regulated (*Acy3*) genes, all other genes were consistent with the RNA-seq data (Supplementary Fig. S3A).

3.3. Mobilization of immune response genes is the most prominent feature among the upregulated DEGs in the SGs of DIO mice

To gain insight into the specific pathways and genes affected in the SGs of the DIO mice, we performed a GO analysis of the up- and down-regulated DEGs in the DIO mice. GO analysis of the 543 upregulated DEGs (Fig. 3A) in the DIO mice using the biological process (BP) term showed that all the top 10 categories were related to immune response (together 231 genes, ∼42.5 % of the 543 upregulated DEGs), including innate immune response, adaptive immune response and immune response process (Fig. 3B, BP panel; Supplementary Table S6). In the cellular component (CC term), 8 out of the top 10 categories were related to extracellular proteins, membrane proteins or their trafficking (together 349 genes, ∼64.3 % of the 543 upregulated DEGs) (Fig. 3B, CC panel; Supplementary Table S7). Cross-comparison of the genes in the top 10 categories in the BP and CC terms identified 220 DEGs to be shared (Supplementary Table S8). These 220 DEGs are mainly
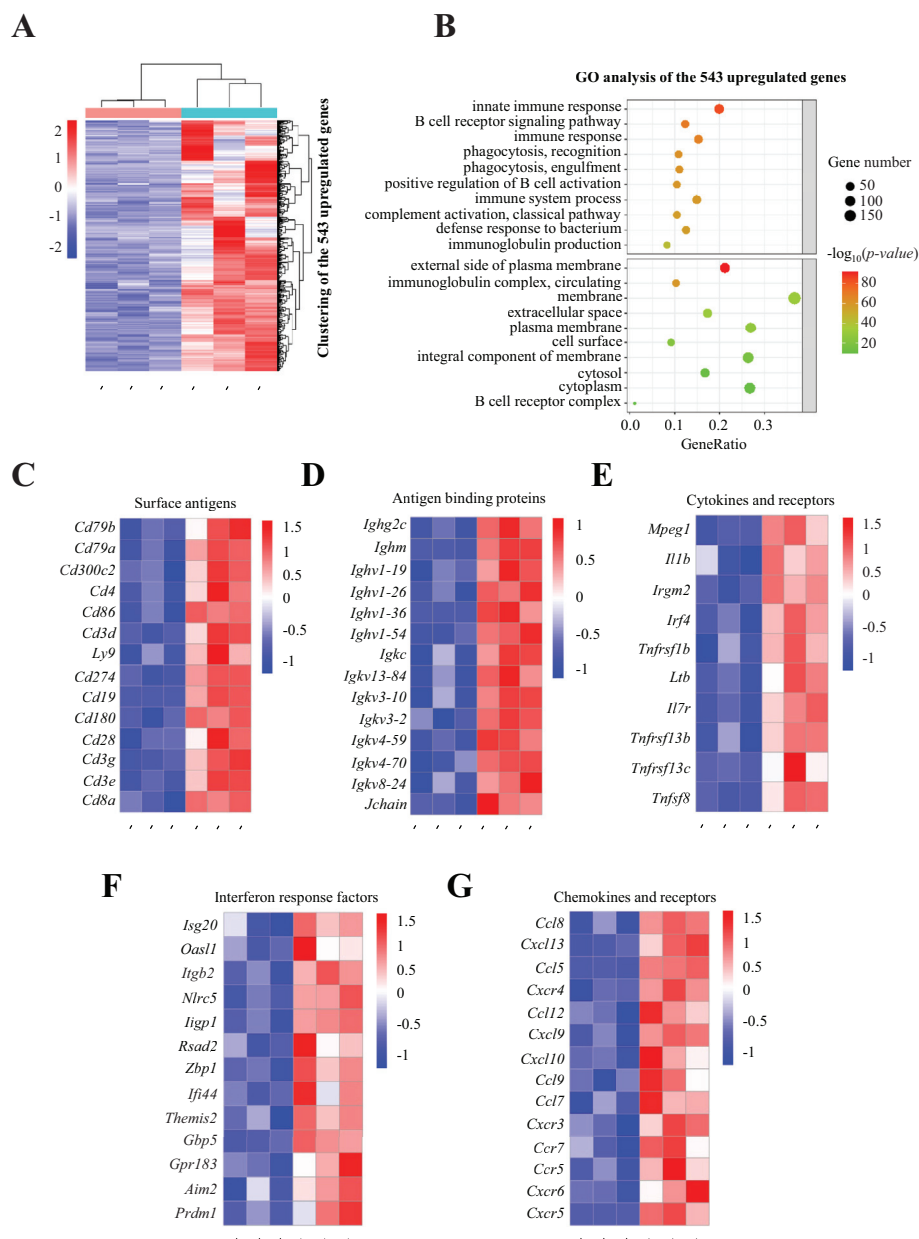
Fig. 3. GO analysis of the upregulated DEGs shows that mobilization of the immune response genes is the most significant change in the SGs of DIO mice. (A) Heatmap showing the 543 upregulated DEGs in the DIO mice (DIO-1, -2 and -3) compared with the three NC mice (NC-1, -2 and -3). (B) Bubble graph showing the top 10 categories of the GO analysis of the DIO upregulated DEGs under the BP and CC GO terms (gene list for each category: Supplementary Tables S6 and S7). Size of the circle, indicating the number of genes in each GO; color of the circle, -$\log_{10}$ value (*p*-adjust) as indicated in the color bar. (C-G) Heatmaps comparing the representative upregulated DEGs between DIO mice (DIO-1, -2 and -3) and NC mice (NC-1, -2 and -3), including surface antigens (C), antigen binding proteins (D), cytokines and receptors (E), interferon response factors (F), chemokines and their receptors (G). Heat bar: value of $\log_2$(TPM).

responsible for a variety of immune responses, including genes encoding surface antigens (*Cd28*, *Cd3d*, *Cd3g*, *Cd4*, *Cd8a*, *Cd8b1*, *Cd19*, *Cd38*, *Cd79a*, *Cd79b*, *Cd84*, *Cd86*, *Cd180*, *Cd274*, *Ly9* etc) (Fig. 3C, Supplementary Table S8), antigen binding proteins (*Ighg2c*, *Ighm*, *Ighv1-26*, *Ighv1-36*, *Ighv1-53*, *Ighv1-54*, *Ighv1-74*, *Ighv1-61*, *Ighv1-62–2*, *Ighv1-64*, *Ighv1-66*, *Ighv1-78*, *Ighv2-2*, *Ighv3-6*, *Ighv5-4*, *Ighv5-6*, *Ighv5-9*, *Ighv7-1*, *Igkc*, *Igkv3-2*, *Igkv3-10*, *Igkv4-57–1*, *Igkv4-59*, *Igkv4-70* etc) (Fig. 3D, Supplementary Table S8), cytokines and receptors (*Il1b*, *Il7r Itgb2*, *Ltb*, *Mpeg1*, *Tnfrsf1b*, *Tnfrsf13b*, *Tnfrsf13c*, *Tnfrsf14*, *Tnfsf8* etc) (Fig. 3E, Supplementary Table S8), interferon response factors (*Aim2*, *Gbp5*, *GPr183*, *Ifi44*, *Iigp1*, *Isg20*, *Nlrc5*, *Oasl1*, *Prdm1*, *Rsad2*, *Themis2*, *Zbp1* etc) (Fig. 3F, Supplementary Table S8), and chemokines and their receptors (*Ccl5*, *Ccl6*, *Ccl7*, *Ccl8*, *Ccl9*, *Ccl12*, *Ccr5*, *Ccr7*, *Cxcl9*, *Cxcl10*, *Cxcl13*, *Cxcr3*, *Cxcr4*, *Cxcr5*,

Cxcr6 etc) (Fig. 3G, Supplementary Table S8). The up-regulation of 17 immune response related genes, including *Cd4*, *Cd8a* and *Cd79a*, were confirmed by the qPCR (Fig. S3B). The elevation of CD4, CD8A and CD79A protein levels in the salivary glands of DIO mice were confirmed by both immunohistochemical staining (Fig. 4A-C) and western blotting analysis (Fig. 4D). The above analysis strongly suggests that obesity triggers an activation of the immune response genes in the SGs of DIO mice.

3.4. Genes related to exocrine activities were downregulated in the SGs of DIO mice

For the 212 down-regulated DEGs (Fig. 5A), 7 out of the top 10 categories in the CC term were related to the secretory pathways
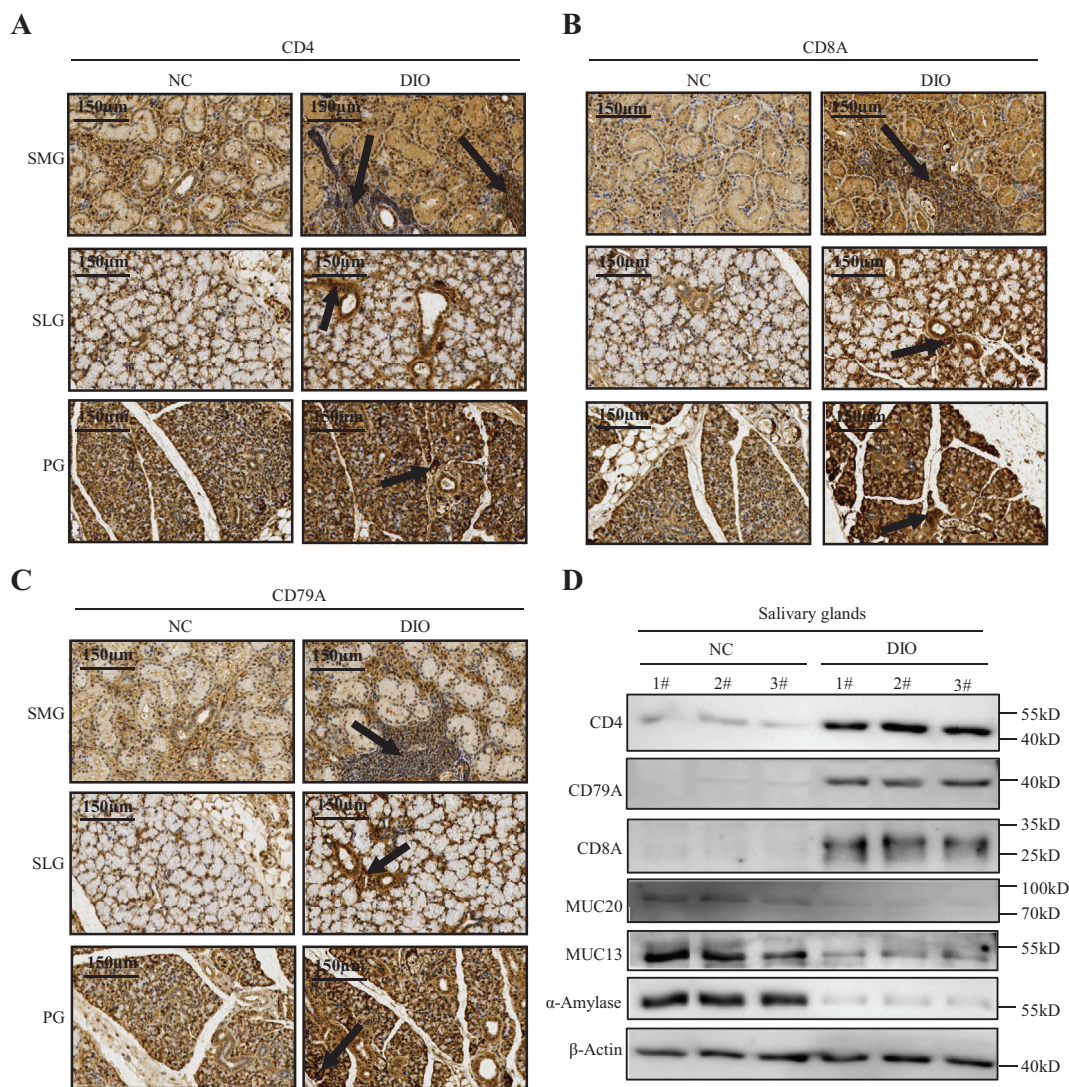
Fig. 4. The levels of immune response related proteins were elevated in the SGs of DIO mice. (A-C) Immunohistochemical analysis of CD4 (A), CD8 (B) and CD79A (C) in the SMG, SLG and PG from the NC and DIO mice (week-35), respectively. Arrow points to the representative region with elevated protein positive signals in the DIO mice. (D) Western blot analysis of CD4, CD79A, CD8A, MUC20, MUC13 and α-Amylase in the SGs of three NC mice and three DIO mice (week-35), respectively. β-Actin: loading control.

(extracellular matrix, cell membrane and recycling endosome) (together 116 genes, ~54.7 % of the 212 downregulated DEGs) (Fig. 5B, Supplementary Table S9). Although the secretory pathways were among the prominent categories in both up- and down-regulated genes in the CC term, detailed analysis revealed that the upregulated DEGs encoded secretory proteins mainly related to immune response, including immunoglobulins, surface antigens, cytokines and their receptors and signaling, and chemokine and their receptors (Fig. 3C-G, Supplementary Tables S7 and S8). In contrast, the downregulated DEGs encode mainly membrane channels or transporters for water (*Aqp2*), anion (*Bsnd*, *Clcnka*), cation (*Hcn2*, *Kcnip2*, *Kcnj8*, *Scnn1g*, *Tmem37*), sugar (*Slc2a4*), and peptide (*Tmem158*) (Fig. 5C, Supplementary Table S9), extracellular matrix components (*Adamts2*, *Adamts10*, *Adamts17*, *Colca2*, *Emid1*, *Fmod*, *Pm20d1*, *Tsku*, *Ucma* etc) (Fig. 5D, Supplementary Table S9), ligands and their perception and signaling (*Ardb1*, *Efna4*, *Efnb1*, *Fgfbp3*, *Fzd10*, *Inha*, *Mdk*, *Nrtn*, *P2rx3*, *Sema3b*, *Tfr2* etc) (Fig. 5E, Supplementary Table S9), and protein trafficking and cycling endosome (*Gal3st3*, *Pheta1*, *Porcn*, *Rab17*, *Rin1*, *Snca*, *Snx21*, *St6galnac2* etc) (Fig. 5F, Supplementary Table S9). Downregulation of these genes suggests that obesity appears to compromise the secretory function of the SGs in DIO mice. Interestingly, *Cntfr*,

Ngef and *Nrep* genes involved in synaptic function were also among the downregulated genes (Supplementary Table S9), suggesting that obesity might also have an effect on the neuronal regulation of the SG functions.

The top 10 categories in the BP term for the 212 downregulated DEGs were diversified, including processes related to cell differentiation, negative cell growth, multicellular organ development etc (Fig. 5B, Supplementary Table S10), which might explain the compromised cellular function of the SGs in DIO mice although there was no obvious morphological changes. In addition, three genes related to cold-response pathways (*Adrb1*, *P2rx3* and *Ucp3*) were also downregulated (Fig. 5G). Interestingly, we found that three genes regulating circadian rhythm, namely *Per2*, *Per3* and *Nr2f6* were downregulated in the DIO mice (Fig. 5H). This data suggests that obesity might lead to energy production and sleeping disorders apart from causing abnormal immune response and exocrine activity.

To find out whether downregulation of genes related to secretory activities would affect the secretion of extracellular matrix proteins in the DIO mice, we stained the NC and DIO mice with Alcian blue. The result showed that the staining signals of the extracellular matrix appeared to be reduced in all three major
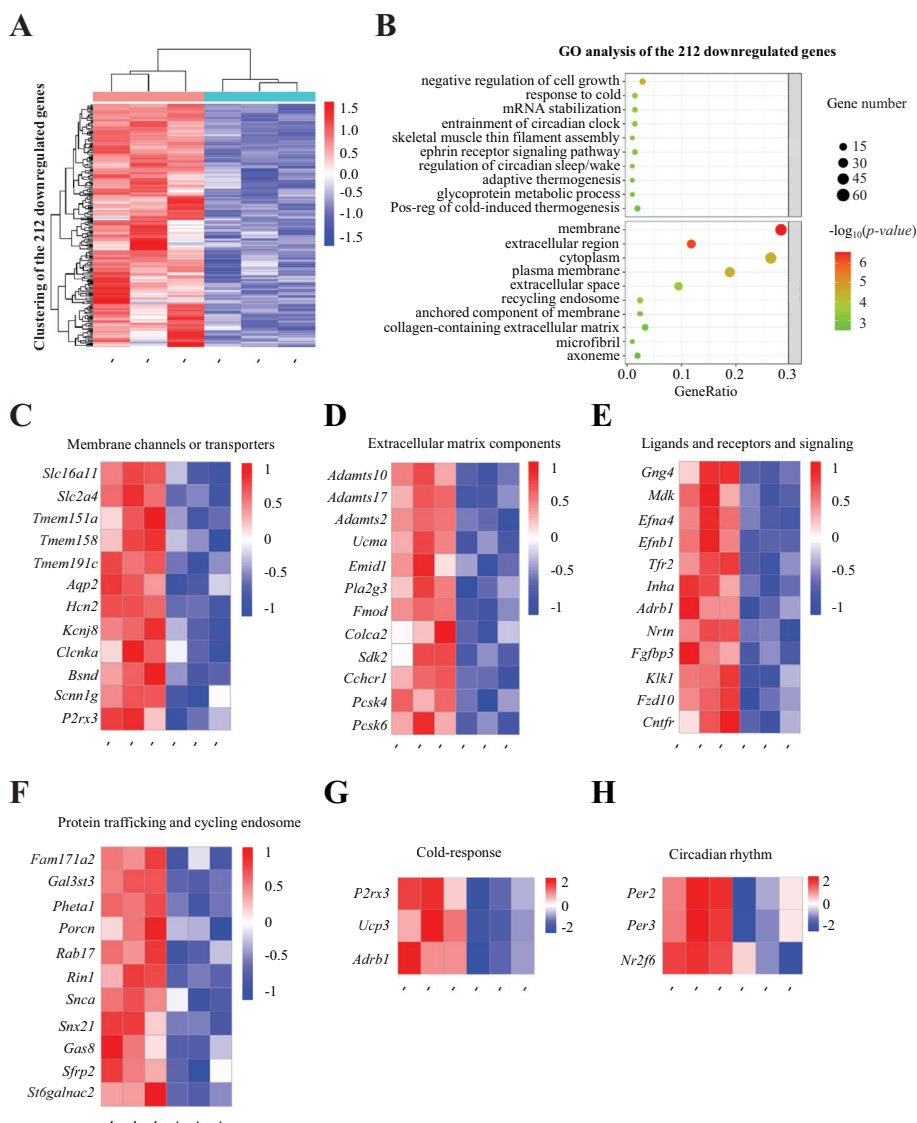
Fig. 5. Compromise of the secretory pathway genes is the most significant feature in the SGs of DIO mice for the DIO downregulated DEGs. (A) Heatmap showing the 212 downregulated DEGs in the DIO mice (DIO-1, -2 and -3) compared with the NC mice (NC-1, -2 and -3). (B) Bubble graph showing the top 10 categories of the GO analysis of the DIO downregulated DEGs under the BP and CC GO terms (gene list for each category: Supplementary Tables S9 and S10). (C–H) Heatmaps showing the representative downregulated DEGs related to membrane channels/transporters (C), extracellular matrix components (D), ligands and their receptors and signaling (E), protein trafficking and recycling endosome (F), cold response (G) and circadian rhythm (H). Heat bar: value of log$_2$(TPM).

SGs in the DIO mice, especially PG which showed approximately twofold reduction (Fig. 6A-C). Western blot analysis showed that the production of MUC20, MUC13 and α-Amylase was obviously reduced in the SGs of the DIO mice compared with that in the NC mice (Fig. 4D). In addition, the DIO mice showed a reduced stimulated saliva flow rate (Fig. 6D) and a subtle but significant elevation in the peroxidase activity (Fig. 6E). Furthermore, the stimulated saliva from the DIO mice contained less Mucin 13 and α-Amylase than that from the NC mice (Fig. 6F). These results are consistent with previous report in both obese mice and human [13–17].

3.5. scRNA-seq analysis identified 17 cell clusters in SLG

In murine, SMG is the largest glands (~75 % mass of all SGs), followed by PG (~15 %) and SLG (~8%). The scRNA-seq approach has been adopted to analyze the cell types and their changes in SMG during SG development or in response to the condition of Sjögren's

Syndrome (SS) [1,7,8,10,32]. For PG, one murine report determined the cell types for young mouse (18 days postnatal) based on 492 cells characterized[8], and a recent report identified 10 cell types in human parotid with majority of cells being T and B cells [6]. For SLG, however, currently there is no report on cell typing based on scRNA-seq analysis.

We dissected SMG, SLG and PG from the NC mice (SMG combined from 3 mice and SLG one mouse at 35 weeks postnatal, PG from one mouse at 40 weeks postnatal) and from the DIO mice (SMG combined from 3 mice and SLG from one mouse at 35 weeks postnatal, PG from one mouse at 40 weeks postnatal), respectively, for scRNA-seq analysis (Supplementary Table S11). In total, 5689, 2416 and 1491 cells for SMG, SLG and PG from the NC mice, 6545, 3254 and 1917 cells for SMG, SLG and PG from the DIO mice, passed the quality control criteria (Supplementary Fig. S4A-F). PCs for cell clustering were determined by the ElbowPlot provided by the Seurat package (Supplementary Fig. S4G). Cells were clustered using the unsupervised clustering with affinity propagation based
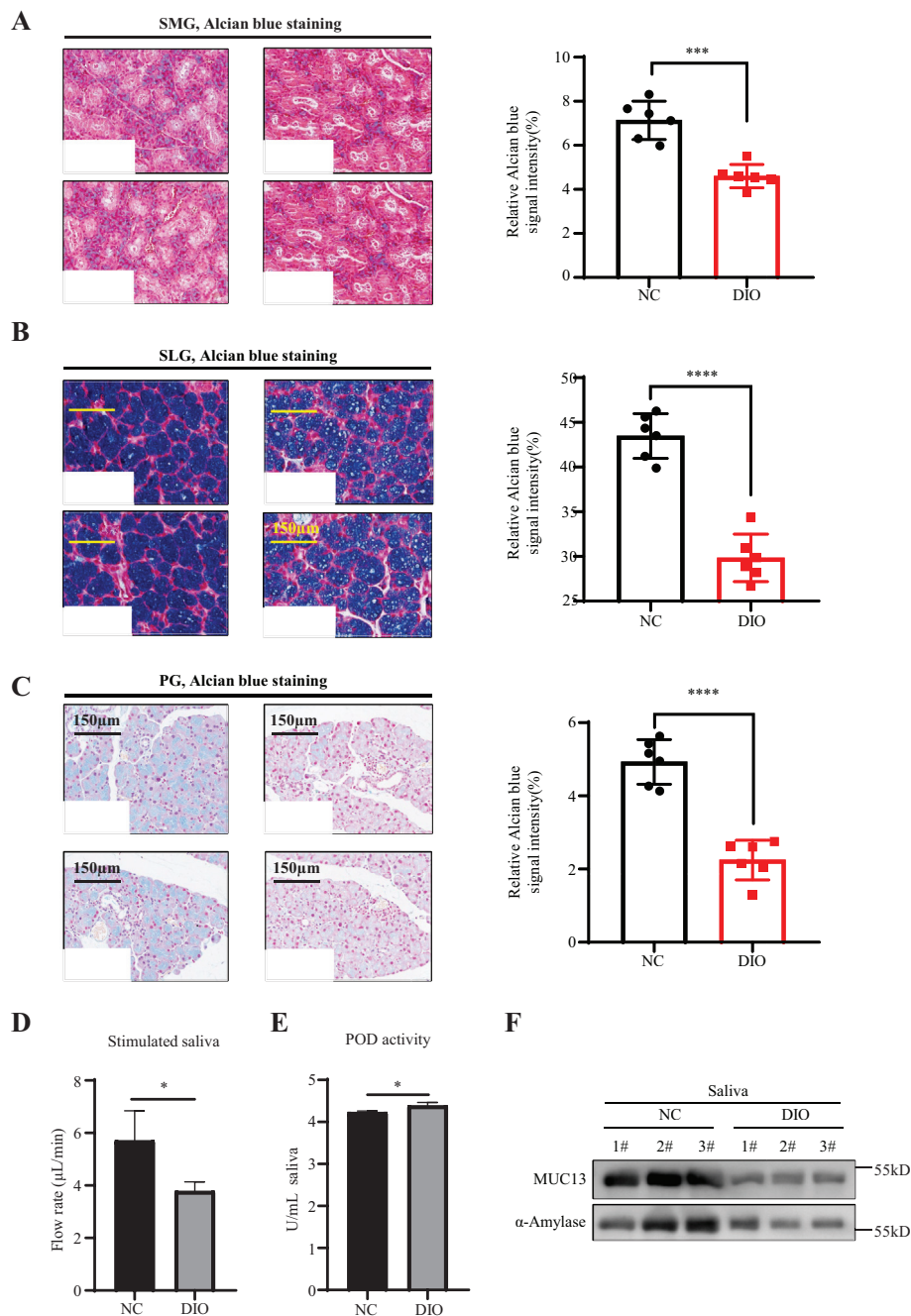
Fig. 6. SGs of the DIO mice produced less mucin. (A-C) Images showing the alcian blue staining of sections of the SMG (A), SLG (B) and PG (C) dissected from NC-2, NC-3, NC-7, NC-8, DIO-2 and DIO-3, DIO-7 or DIO-8 as indicated. Statistic comparison of the relative staining intensity (ratio of the blue color pixels against total color pixels) between NC and DIO mice is shown on the right. Blue staining signals of 2 sections from each NC (NC-2, NC-3, NC-7, and NC-8) and DIO (DIO-2, DIO-3, DIO-7 and DIO-8) mice were acquired for statistic analysis. (D-F) Comparing the pilocarpine hydrochloride stimulated saliva flow rate (n = 3) (D), peroxidase (POD) activity (n = 3) (E) and proteins levels of MUC13 and α-Amylase in the stimulated saliva between three NC and three DIO mice (week-35). For (F), equal amount of the loaded protein samples was determined based on the protein concentration measured using the Bradford method. ***, $p < 0.001$; ****, $p < 0.0001$.

on the expression of high-variance genes (Supplementary Fig. S5A-C, Table S12) and cell clusters were plotted with the uniform manifold approximation and projection (UMAP) figure.

For 5670 SLG cells combined of the NC and DIO mice, 17 clusters were identified (Fig. 7A, Supplementary Fig. S5B). Annotation of these 17 clusters with feature genes [1,7–10,32–37] (Supplementary Table S12 and S13) identified serous (cluster 4), seromucous (cluster 6) and mucous (cluster 11) three types of acinar cells, and striated (cluster 1), intercalated (cluster 7), excretory (cluster 8) and GCT (cluster 9) four types of ductal cells (Fig. 7A, Supplementary Fig. S5B). Dot plot and violin plot showed that, *A2ml1*

and *Smgc* were enriched in mucous cells, so were *Bpifa2* and *Dcpp1* in serous cells, *Car6* and *2310057J18Rik* in seromucous cells, *Sult1c1* and *Atp6v1g3* in excretory and striated ductal cells, *Cyp2f2* and *Esp18* in intercalated ductal cells, and *Egf* and *Klk1b8* in GCT cells (Fig. 7B-C). These genes could serve as marker genes for these cell types in the SLG. The rest clusters included stromal cells (cluster 12), endothelial cells (cluster 13) and various immune cells (Fig. 7A, Supplementary Fig. S5B and Table S13). To validate our scRNA-seq data, we adopted the CIBERSORTx tool [25] to analyze the expression of 1261 feature genes (identified by our scRNA-seq) in a publicly available NC mouse SLG RNA-seq dataset (male,
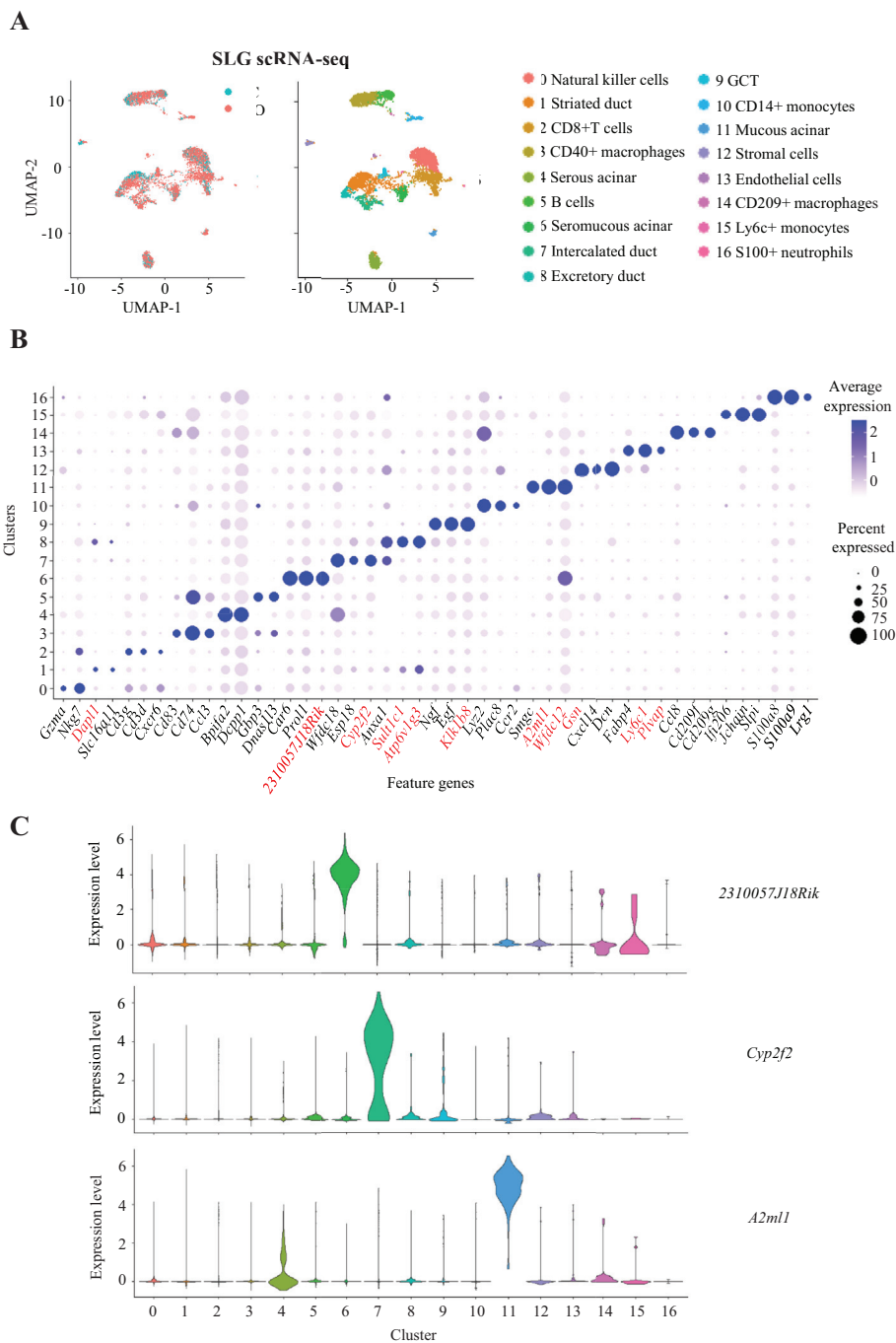
Fig. 7. Identification of 17 distinct cell clusters in the SLG. (A) UMAPs showing the 17 cell clusters identified in SLG by scRNA-seq. 2416 cells from NC-5 mouse and 3254 from DIO-5 mouse were combined for the analysis. Left UMAP, superimpose of NC and DIO cells; right UMAP, 17 cell clusters marked with corresponding number. Cluster identity is shown on the right. (B-C) Dot plot (B) and violin plot (C) identified marker genes for different acinar cell and ductal cells as shown (*A2ml1* and *Smgc* for mucous acinar; *Bpifa2* and *Dcpp1* for serous acinar; *Sult1c1* and *Atp6v1g3* for striated/excretory duct; *Cyp2f2* and *Esp18* for intercalated duct; *Anxa1* for excretory duct; *Egf* and *Klk1b8* for GCT). In B, gene name in black represents the admitted marker genes reported previously (Supplementary Table S12), gene name in red represents the new feature gene identified in this study.

12 weeks age) [26]. Deconvolution analysis of these feature genes in the clustered 2416 SLG cells obtained from the NC mouse revealed a largely nice correlation between our scRNA-seq data and the published SLG RNA-seq regarding the compositions of different cell types (Supplementary Fig. S6A). However, we noticed that the compositions of mucous acinar and serous acinar two cell types were more highly represented by the published dataset (Supplementary Fig. S6A). Whether this is due to the age difference (12

vs 35 weeks) for sampling or a genuine methodology difference or individual mouse variations needs to explored in the future.

For 12,234 SMG cells combined of the NC and DIO mice, 16 clusters were well defined (Supplementary Fig. S5A and S6B). Annotation with feature genes (Supplementary Table S12 and S13) identified seromucous (cluster 3) and serous (cluster 4) two types of acinar cells, and GCT (cluster 5), striated (cluster 6) and intercalated (cluster 7) three types of ductal cells in the SMG

(Supplementary Fig. S5A and S6B), which nicely coincided with previous reports [1,7,8,10,32]. Dot plot confirmed the known SMG serous acinar markers *Aqp5* and *Lpo*, serous and seromucous acinar markers *Wfdc12* and *Car6*, intercalated duct marker *Esp18*, striated duct marker *Fxyd2* and *Ascl3*, and GCT markers *Egf* and *Ngf* [1,7,8,10,32] (Supplementary Fig. S7A-B). Meanwhile, dot plot and violin plot identified putative new markers for SMG serous acinar (*A630073D07Rik*), intercalated duct (*Cyp2f2*), striated duct (*Atp6v1g3*) and GCT (*Klk1b1*), respectively (Supplementary Fig. S7-B-C).

For 3408 PG cells combined of the NC and DIO mice, 9 clusters were identified (Supplementary Fig. S5C and S6C). Annotation with feature genes (Supplementary Table S12 and S13) identified serous (cluster 0), mucous (cluster 1), Mucl2+ (cluster 2) and seromucous (cluster 6) four types of acinar cells, and striated (cluster 3) and intercalated (cluster 4) two types of ductal cells (Supplementary Fig. S5C and S6C). Dot plot confirmed the known PG serous acinar
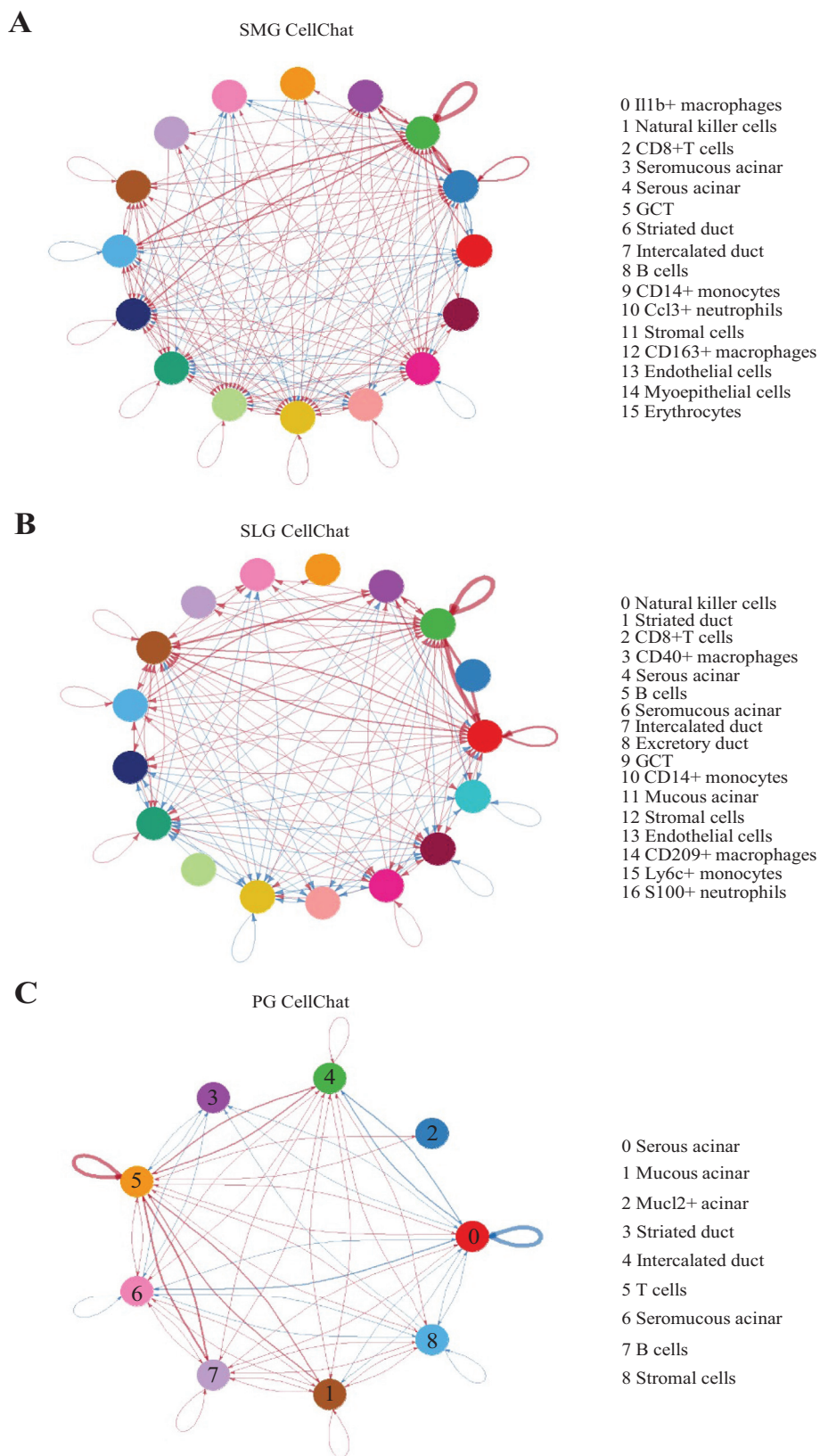
markers *Prol1* and *Bpifa2*, seromucous acinar markers *Dcpp1* and *Dcpp2*, Mucl2+ acinar marker *Mucl2*, striated duct marker *Esp4*, and intercalated duct marker *Wfdc18* [1,7,8,10,32] (Supplementary Fig. S8A-B). Dot plot and violin plot also identified putative new markers for PG serous acinar (*Scgb2b27*), Mucl2+ acinar (*Scgb1b2* and *Scgb1b29*), striated duct (*Gm5938* and *Mup4*) and intercalated duct (*Sftpd* and *Cyp2f2*), respectively (Supplementary Fig. S8B-C).

3.6. scRNA-seq analysis reveals an enhanced recruitment of immune cells into SMG, SLG and PG in DIO mice

The scCODA method [28] was adopted to estimate the relative change in the cell compositions in the SMG, SLG and PG cells between NC and DIO mice, respectively (Fig. 8A-C). The ratios of T and B cells were found to display a significant increase in all three SGs (DIO vs NC, in SMG: 19.3 % vs 6.5 % for CD8$^+$ T cells, 9.9 % vs 4 % for B cells; in SLG: 10 % vs 5.8 % for CD8$^+$ T cells, 2.9 % vs 1.7 % for B
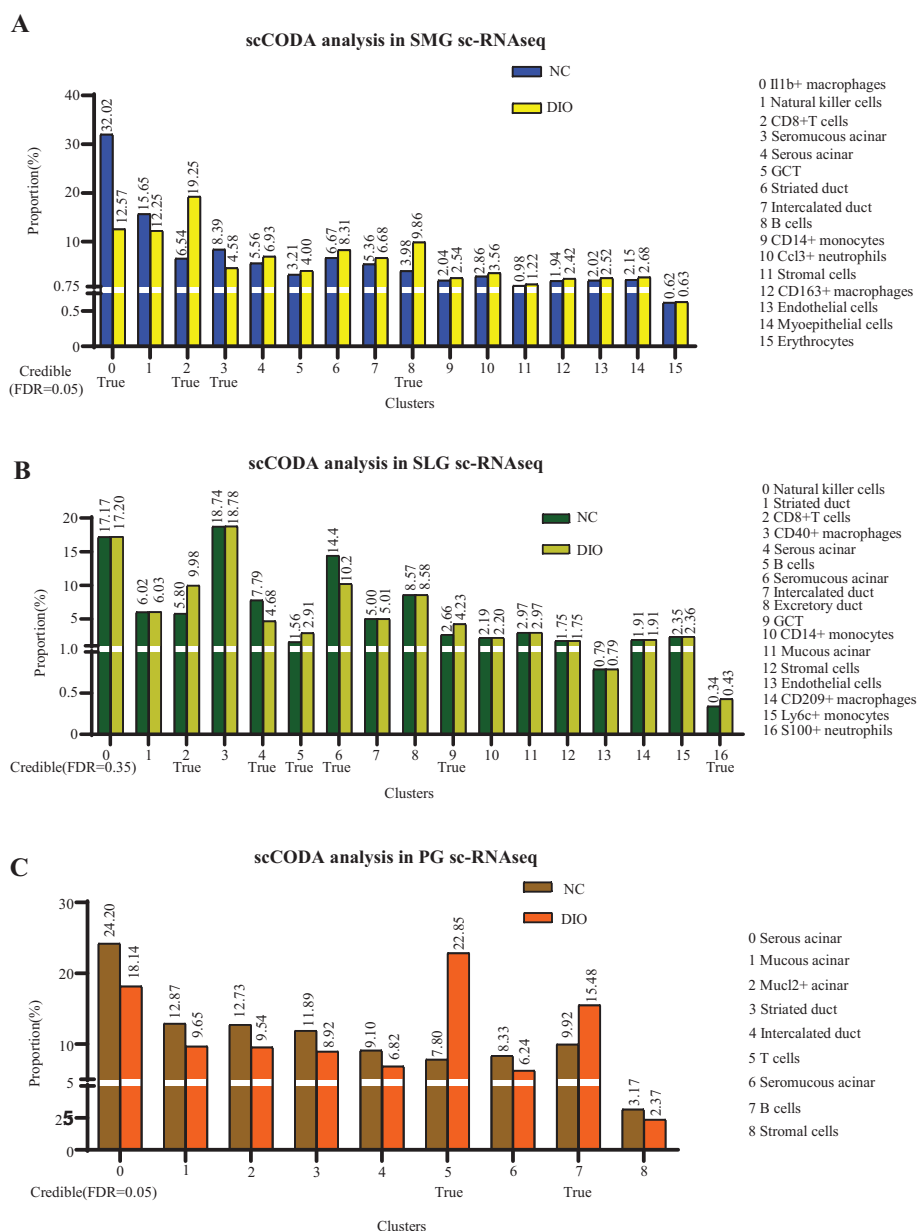
Fig. 8. SGs exhibited an increased ratio of T and B cells in DIO mice. (A-C) Histogram showing the pairwise comparison of the ratios of each cell cluster in the SMG (A), SLG (B) and PG (C) between NC and DIO mice. The scCODA method was adopted for this analysis and credible false discovery rate (FDR) is provided for each SGs as shown. Only the cell clusters satisfied the credible FDR criteria with reference to the stromal cells are highlighted as 'true' in the graph. Cluster identity for each SGs is shown on the right. Pairwise comparison Ratios.

A

SMG CellChat

0 Il1b+ macrophages
1 Natural killer cells
2 CD8+T cells
3 Seromucous acinar
4 Serous acinar
5 GCT
6 Striated duct
7 Intercalated duct
8 B cells
9 CD14+ monocytes
10 Ccl3+ neutrophils
11 Stromal cells
12 CD163+ macrophages
13 Endothelial cells
14 Myoepithelial cells
15 Erythrocytes

B

SLG CellChat

0 Natural killer cells
1 Striated duct
2 CD8+T cells
3 CD40+ macrophages
4 Serous acinar
5 B cells
6 Seromucous acinar
7 Intercalated duct
8 Excretory duct
9 GCT
10 CD14+ monocytes
11 Mucous acinar
12 Stromal cells
13 Endothelial cells
14 CD209+ macrophages
15 Ly6c+ monocytes
16 S100+ neutrophils

C

PG CellChat

0 Serous acinar
1 Mucous acinar
2 Mucl2+ acinar
3 Striated duct
4 Intercalated duct
5 T cells
6 Seromucous acinar
7 B cells
8 Stromal cells

Fig. 9. The cells in the SMG, SLG and PG of the DIO mice exhibited a stronger interaction initiated by the immune cells. (A-C) Circle plot showing directional interactions among the identified cells in the SMG (A), SLG (B) and PG (C) based on the analysis using the CellChat method. The width of the edge indicates the relative interaction strength. Red and blue colored edges represent increased and decreased interaction strength, respectively, in the DIO compared to the NC. Cell cluster annotation is shown on the right.

cells; in PG: 22.9 % vs 7.8 % for T cells, 15.5 % vs 9.9 % for B cells) (Fig. 8A-C). Interestingly, macrophages appeared to be reduced in the DIO SMG (DIO vs NC: 12.6 % vs 32 %). In contrast, the ratios of the seromucous acinar cells were significantly reduced in SMG and SLG in DIO mice (DIO vs NC, SMG: 4.6 % vs 8.4 %; SLG: 10.2 % vs 14.4 %) (Fig. 8A-C), indicative of compromised SG secretory functions in DIO mice [18,38].

3.7. Cell-cell interaction analysis confirms a stronger immune response in the DIO mice

Next, based on the scRNA-seq data we analyzed the cell–cell interactions in SMG, SLG and PG, respectively, and compared the cell–cell interaction differences between the NC and DIO mice for each gland by adopting the CellChat tool [27] (Supplementary Tables S14-S19). The list of significant interaction pathways is provided in Supplementary Table S20. For SMG, the number of inferred interactions for the NC and DIO cells was not drastically different, being 889 and 914 (Supplementary Fig. S9A, left panel; Tables S14 and S15), respectively, however, the DIO cells showed a stronger interaction strength (0.02) than that did the NC cells (0.005) (Supplementary Fig. S9B, left panel). Rank significant signaling networks based on the information flow identified the cytokine-cytokine receptor (CXCL) and ECM-receptor (FN1) two CellChat pathways to be unique to the NC cells while nine CellChat pathways (including CDH, CD200, PECAM1, SELL, SELPLG and CD48) were unique to the DIO cells (Supplementary Fig. S9C, left panel). The other eight significant CellChat pathways were stronger in the DIO cells (Supplementary Fig. S9C, left panel). The interaction output among different cell clusters showed an enhanced interaction between CD8$^+$ (cluster 2) and B cells (cluster 8) and between CD8$^+$ and CD14$^+$ cells (cluster 9). CD8 + cells also displayed a strong self-interaction (Fig. 9A).

For SLG, 670 and 415 inferred interactions were identified for the NC and DIO cells (Supplementary Fig. S9A, middle panel; Tables S16 and S17), respectively, where the DIO cells showed a much stronger interaction index (0.011) than the NC cells (0.002) (Supplementary Fig. S9B, middle panel). Five significant CellChat pathways (CCL, JAM, EGF, CSF and CDH) were assigned to the NC cells while APP and IL2 two pathways were unique to the DIO cells (Supplementary Fig. S9C, middle panel). Meanwhile, MHC-1 and CD48 two pathways were more prominent in the DIO cells (Supplementary Fig. S9C, middle panel). Regarding the interactions among different cell clusters, CD8$^+$ cells (cluster 2), as in the SMG, again showed an strong self-crosstalk (Fig. 9B). CD8$^+$ cells also showed a strong interaction with the NK cells (cluster 0) and appeared to affect the intercalated duct cells (cluster 7) (Fig. 9B).

For PG, much less inferred interactions were identified by Cell-Chat, being 297 and 329 for the NC and DIO cells, respectively (Supplementary Fig. S9A, right panel; Tables S18 and S19). Although the interaction strength was slightly stronger for the DIO cells (0.005) than that for the NC cells (0.003) (Supplementary Fig. S9B, right panel), the magnitude of the strength for the DIO cells was much weaker compared with the SMG and SLG (Supplementary Fig. S9B). Much less significant CellChat pathways were identified for the PG cells, with three pathways (THBS, COLLAGEN and FN1) being unique to the DIO cells and the CDH and CSF two pathways to the NC cells (Supplementary Fig. S9C, right panel). As in the SMG and SLG, T cells (cluster 5) in the DIO showed a strong self-interaction (Fig. 9C). The T cells also showed certain interactions with B cells (cluster 7) and mucous acinar cells (cluster 1). Interestingly, the serous acinar cells in the NC cells displayed a prominent self-interaction (Fig. 9C), which was not observed in the SMG and SLG (Fig. 9A-B). The cell–cell interaction analysis confirmed that the immune response was activated in the SGs in the DIO mice.

4. Discussion

Extensive studies have demonstrated the vital role of SGs in maintaining mouth health and facilitating food digestion as an exocrine tissue [4,5,39,40], however, only limited efforts have been spent on exploring the effect of obesity on the function of SGs [13,14,16,18]. In this report, we started with the bulk RNA-seq approach to study the effect of obesity on gene expression profiles in the DIO mice. We identified a total of 755 DEGs, including 543 upregulated and 212 downregulated DEGs, approximately 4 % of the total detected genes. GO analysis of the upregulated DEGs showed that the most prominent feature is the upregulation of more than 231 immune response related genes in the SGs of DIO mice. Based on the GO analysis, these genes are known to take part in multiple immune response pathways, including innate immune response, adaptive immune response and immune cell differentiation and maturation. In human, it is generally perceived that excessive and abnormal accumulation of fat in obese patients will trigger the generation of pro-inflammatory factors, such as Leptin, various cytokines, Adiponectin and various chemokines that circulate in the body to reach the target tissues to cause chronic inflammation [41–45]. Obesity-induced inflammation has been related to the initiation and development of cancer [43], nonalcoholic fatty liver disease (NAFLD) [44], neurodegenerative diseases [41] and metabolic disorders [42,45]. Our results demonstrate that the SGs are also subjected to chronic inflammation in the obese mice. Interestingly, among the 755 DEGs (mouse genes), 604 have been assigned with corresponding human counterparts (using the Profiler utility provided by the ESEMBL database) (Supplementary Table S21). Considering the above fact, we believe the data obtained in this study could serve as a reference for studying whether the SGs also suffer from a chronic inflammation by upregulating a similar group of genes in obese human patients in the future.

Extracellular matrix connects and supports the acinar and ductal systems within the glands which facilitates the saliva secretion [4,5]. We found that the majority of the downregulated DEGs encode proteins belonging to extracellular matrix components, membrane channel proteins for import and export of water, anion and cations, membrane receptors for different ligands, and proteins involved in protein trafficking and endocytosis. These changes suggest that the exocrine function of the SGs of DIO is likely compromised. Indeed, our data showed that the deposition of the extracellular matrix, the stimulated saliva flow rate and the content of mucin in the saliva was found to be reduced in the SGs of DIO mice. In human, studies have shown that overweight or obese adolescents exhibited a significant less saliva and total protein secretion after stimulation [14,15,17]. Whether the reduced saliva secretion in human is also a consequence of downregulation of genes encoding proteins for import and export of water, anion and cations, and for proteins trafficking in the SGs is worth to be explored in the future.

Circadian genes play essential roles in controlling or regulating animal development, physiology and behavior [46]. The expression of circadian genes is largely controlled by a regulatory network formed by the transcriptional regulators including BMAL1, CLOCK, PER and CRY [47]. It has been reported that obesity affects the cellular rhythmic response in a range of tissues. For example, using a transgenic reporter mice *PER2::luciferase*, Larion and colleagues found that *PER2* lost its normal rhythmic expression pattern and its expression level in the liver was reduced at 24:00 h in the *db/db* obese mice [47]. In human, epigenetic studies showed that *CLOCK*, a positive regulator of *PER2*, was highly methylated at its promoter in the white cells obtained from overweight and obese women and the baseline methylation of *CLOCK* was correlated with the level of wight-loss in these women [48]. In children with the

obesity trait, whole genome epigenetic studies of the white blood cells revealed a negative correlation between the methylation of PER3 in the gene body region with the body mass index (BMI) [49]. The downregulation of *Per2*, *Per3* and *Nr2f6* in the DIO mice suggests that obesity might disrupt the cellular circadian rhythm in the salivary glands as well.

It is well known that SMG, SLG and PG three major SGs play similar and also distinct functions, which is clearly reflected in their histologic structures [7,10,32,50]. Establishment of the cell atlas for these three major SGs provides a foundation for understanding their similar and distinct functions. We applied scRNA-seq to determine the cell types within these three major SGs. For SMG and PG, consistent with previous reports [1,7,8,10,32], 16 and 9 cell clusters are identified. We identified, for the first time, 17 cell clusters in SLG and assigned feature genes for these 17 clusters. We suggest *A2ml1*, *Car6*, *Cyp2f2* and *Sult1c1* to be the characteristic gene for mucous acinar, seromucous, intercalated duct and excretory duct in SLG, respectively.

As the first report, we used the scRNA-seq approach to compare the effect of obesity on the cell compositions in SMG, SLG and PG in DIO mice, respectively. We found that the number of immune cells, especially the T and B cells, were significantly increased in all three major SGs in DIO mice. Consistently, cell–cell interaction analysis using the CellChat tool revealed significant enhanced crosstalk among different immune cells and also between immune cells and acinar or ductal cells in the DIO cells. Interestingly, both SMG and SLG cells from the DIO mice exhibited more prominent interactions related to multiple pathways while the PG appeared to be less complicate, suggesting that three SGs might have different ways in response to obesity. These observations further support the conclusion that immune response pathways are mobilized which might lead to a compromised secretory function in the SGs of DIO mice.

It is generally conceived that high energy diet represents one of the greatest environmental factors to induce obesity [12,51]. Our results shown here suggest that controlling immune response and chronic inflammation might be an effective approach to reduce the effect of obesity on the function of SGs in obese patients.

Ethical approval

All animal procedures were performed in full accordance with the Guide for the Care and Use of Laboratory Animals and were approved by the Animal Ethics Committee in Zhejiang University (approved application number: 11871).

CRediT authorship contribution statement

Heping Huang: Data curation, Formal analysis, Investigation, Validation, Writing – review & editing. **Ce Gao:** Methodology, Software, Data curation, Formal analysis, Investigation, Writing – review & editing. **Shuai Wang:** Data curation, Formal analysis, Investigation, Validation, Writing – review & editing. **Fen Wu:** Data curation, Formal analysis, Investigation. **Jinsong Wei:** Data curation, Formal analysis, Investigation. **Jinrong Peng:** Conceptualization, Funding acquisition, Formal analysis, Project administration, Supervision, Writing – original draft, Writing – review & editing.

Declaration of Competing Interest

The authors declare that they have no known competing financial interests or personal relationships that could have appeared to influence the work reported in this paper.

Appendix A. Supplementary data

Supplementary data to this article can be found online at https://doi.org/10.1016/j.csbj.2022.11.054.

References

[1] Horeth E, Oyelakin A, Song EC, Che M, Bard J, Min S, et al. Transcriptomic and single-cell analysis reveals regulatory networks and cellular heterogeneity in mouse primary Sjogren's syndrome salivary glands. Front. Immunol. 2021;12:729040.

[2] Oyelakin A, Horeth E, Song EC, Min S, Che M, Marzullo B, et al. Transcriptomic and network analysis of minor salivary glands of patients with primary Sjogren's syndrome. Front. Immunol. 2020;11:606268.

[3] Lan X, Chan J, Pu JJ, Qiao W, Pang S, Yang WF, et al. Saliva electrolyte analysis and xerostomia-related quality of life in nasopharyngeal carcinoma patients following intensity-modulated radiation therapy. Radiother. Oncol. 2020;150:97–103.

[4] Mattingly A, Finley JK, Knox SM. Salivary gland development and disease. Wiley Interdiscip. Rev. Dev. Biol. 2015;4(6):573–90.

[5] Suzuki A, Ogata K, Iwata J. Cell signaling regulation in salivary gland development. Cell. Mol. Life Sci. 2021;78(7):3299–315.

[6] Chen M, Lin W, Gan J, Lu W, Wang M, Wang X, et al. Transcriptomic mapping of human parotid gland at single-cell resolution. J. Dent. Res. 2022;101 (8):972–82.

[7] Hauser BR, Aure MH, Kelly MC, Hoffman MP, Chibly AM. Generation of a single-cell RNAseq atlas of murine salivary gland development. iScience 2020;23 (12):101838.

[8] Oyelakin A, Song E, Min S, Bard JE, Kann JV, Horeth E, et al. Transcriptomic and single-cell analysis of the murine parotid gland. J. Dent. Res. 2019;98 (13):1539–47.

[9] Sekiguchi R, Martin D, Yamada KM. Single-cell RNA-seq identifies cell diversity in embryonic salivary glands. J. Dent. Res. 2020;99(1):69–78.

[10] Song EC, Min S, Oyelakin A, Smalley K, Bard JE, Liao L, et al. Genetic and scRNA-seq analysis reveals distinct cell populations that contribute to salivary gland development and maintenance. Sci. Rep. 2018;8(1):14043.

[11] Loos R, Yeo G. The genetics of obesity: from discovery to biology. Nat. Rev. Genet. 2022;23(2):120–33.

[12] van der Klaauw AA, Farooqi IS. The hunger genes: pathways to obesity. Cell 2015;161(1):119–32.

[13] Chielle EO, Casarin JN. Evaluation of salivary oxidative parameters in overweight and obese young adults. Arch Endocrinol Metab 2017;61 (2):152–9.

[14] de Campos MM, Kobayashi FY, Barbosa TS, Costa SS, Lucas BL, Castelo PM. Characteristics of salivary secretion in normal-weight, overweight and obese children: a preliminary study: salivary composition and excessive fat tissue. Odontology 2014;102(2):318–24.

[15] Modeer T, Blomberg CC, Wondimu B, Julihn A, Marcus C. Association between obesity, flow rate of whole saliva, and dental caries in adolescents. Obesity (Silver Spring) 2010;18(12):2367–73.

[16] Roa I, Del SM. Obesity, salivary glands and oral pathology. Colomb. Med. (Cali) 2018;49(4):280–7.

[17] Zalewska A, Kossakowska A, Taranta-Janusz K, Zieba S, Fejfer K, Salamonowicz M, Kostecka-Sochon P, Wasilewska A, Maciejczyk M: Dysfunction of salivary glands, disturbances in salivary antioxidants and increased oxidative damage in saliva of overweight and obese adolescents. J. Clin. Med. 2020, 9(2).

[18] Liu HM, Liu LM, Zhang Y, Cong X, Wu LL, Xiang RL. Integrated analysis of lncRNA and mRNA expression profiles in the submandibular glands of DIO mice. Oral Dis. 2022;28(7):1846–60.

[19] Kim D, Langmead B, Salzberg SL. HISAT: a fast spliced aligner with low memory requirements. Nat. Methods 2015;12(4):357–60.

[20] Love MI, Huber W, Anders S. Moderated estimation of fold change and dispersion for RNA-seq data with DESeq2. Genome Biol. 2014;15(12):550.

[21] Bu D, Luo H, Huo P, Wang Z, Zhang S, He Z, et al. KOBAS-i: intelligent prioritization and exploratory visualization of biological functions for gene enrichment analysis. Nucl. Acids Res. 2021;49(W1):W317–25.

[22] Guan Y, Huang D, Chen F, Gao C, Tao T, Shi H, et al. Phosphorylation of Def regulates nucleolar p53 turnover and cell cycle progression through Def recruitment of Calpain3. PLoS Biol. 2016;14(9):e1002555.

[23] Han X, Wang R, Zhou Y, Fei L, Sun H, Lai S, et al. Mapping the mouse cell atlas by microwell-Seq. Cell 2018;172(5):1091–107.

[24] Jiang M, Xiao Y, Weigao E, Ma L, Wang J, Chen H, Gao C, Liao Y, Guo Q, Peng J, et al. Characterization of the zebrafish cell landscape at single-cell resolution. Front. Cell Dev. Biol. 2021;9.

[25] Newman AM, Liu CL, Green MR, Gentles AJ, Feng W, Xu Y, et al. Robust enumeration of cell subsets from tissue expression profiles. Nat. Methods 2015;12(5):453–7.

[26] Gao X, Oei MS, Ovitt CE, Sincan M, Melvin JE. Transcriptional profiling reveals gland-specific differential expression in the three major salivary glands of the adult mouse. Physiol. Genomics 2018;50(4):263–71.

[27] Jin S, Guerrero-Juarez CF, Zhang L, Chang I, Ramos R, Kuan CH, et al. Inference and analysis of cell-cell communication using Cell Chat. Nat. Commun. 2021;12(1):1088.

[28] Buttner M, Ostner J, Muller CL, Theis FJ, Schubert B. scCODA is a Bayesian model for compositional single-cell data analysis. Nat. Commun. 2021;12 (1):6876.

[29] Baik M, Nam YS, Piao MY, Kang HJ, Park SJ, Lee JH. Liver-specific deletion of the signal transducer and activator of transcription 5 gene aggravates fatty liver in response to a high-fat diet in mice. J. Nutr. Biochem. 2016;29:56–63.

[30] Cho S, Lee H, Han J, Lee H, Kattia RO, Nelson ZV, et al. Viburnum stellato-tomentosum extract suppresses obesity and hyperglycemia through regulation of lipid metabolism in high-fat diet-fed mice. Molecules 2021;26 (4).

[31] Zhao S, Ye Z, Stanton R. Misuse of RPKM or TPM normalization when comparing across samples and sequencing protocols. RNA 2020;26(8): 903–9.

[32] Mauduit O, Aure MH, Delcroix V, Basova L, Srivastava A, Umazume T, et al. A mesenchymal to epithelial switch in Fgf10 expression specifies an evolutionary-conserved population of ionocytes in salivary glands. Cell Rep. 2022;39(2):110663.

[33] Miao N, Zhan Y, Xu Y, Yuan H, Qin C, Lin F, et al. Loss of Fam20c causes defects in the acinar and duct structure of salivary glands in mice. Int. J. Mol. Med. 2019;43(5):2103–17.

[34] Kwak M, Ninche N, Klein S, Saur D, Ghazizadeh S. c-Kit(+) cells in adult salivary glands do not function as tissue stem cells. Sci. Rep. 2018;8(1):14193.

[35] Lo HG, Jin RU, Sibbel G, Liu D, Karki A, Joens MS, et al. A single transcription factor is sufficient to induce and maintain secretory cell architecture. Genes Dev. 2017;31(2):154–71.

[36] Paul F, Arkin Y, Giladi A, Jaitin DA, Kenigsberg E, Keren-Shaul H, et al. Transcriptional heterogeneity and lineage commitment in myeloid progenitors. Cell 2016;164(1–2):325.

[37] Nelson DA, Manhardt C, Kamath V, Sui Y, Santamaria-Pang A, Can A, et al. Quantitative single cell analysis of cell population dynamics during submandibular salivary gland development and differentiation. Biol. Open 2013;2(5):439–47.

[38] Satoh K, Narita T, Matsuki-Fukushima M, Okabayashi K, Ito T, Senpuku H, et al. E2f1-deficient NOD/SCID mice have dry mouth due to a change of acinar/duct structure and the down-regulation of AQP5 in the salivary gland. Pflugers Arch. 2013;465(2):271–81.

[39] Jensen SB, Vissink A, Limesand KH, Reyland ME. Salivary gland hypofunction and xerostomia in head and neck radiation patients. J. Natl. Cancer Inst. Monogr. 2019;2019(53).

[40] Zalewska A, Klimiuk A, Zieba S, Wnorowska O, Rusak M, Waszkiewicz N, et al. Salivary gland dysfunction and salivary redox imbalance in patients with Alzheimer's disease. Sci. Rep. 2021;11(1):23904.

[41] de A BA, de O CP, F FB, E SP, de Moraes L, Migliolo L: Adipose tissue, systematic inflammation, and neurodegenerative diseases. Neural Regen. Res. 2023, 18 (1):38-46.

[42] Kawai T, Autieri MV, Scalia R. Adipose tissue inflammation and metabolic dysfunction in obesity. Am. J. Physiol. Cell Physiol. 2021;320(3):C375–91.

[43] Kolb R, Sutterwala FS, Zhang W. Obesity and cancer: inflammation bridges the two. Curr. Opin. Pharmacol. 2016;29:77–89.

[44] Luo Y, Lin H. Inflammation initiates a vicious cycle between obesity and nonalcoholic fatty liver disease. Immun Inflamm Dis 2021;9(1):59–73.

[45] Saltiel AR, Olefsky JM. Inflammatory mechanisms linking obesity and metabolic disease. J. Clin. Invest. 2017;127(1):1–4.

[46] Zhang R, Lahens NF, Ballance HI, Hughes ME, Hogenesch JB. A circadian gene expression atlas in mammals: implications for biology and medicine. PNAS 2014;111(45):16219–24.

[47] Larion S, Padgett CA, Butcher JT, Mintz JD, Fulton DJ, Stepp DW. The biological clock enhancer nobiletin ameliorates steatosis in genetically obese mice by restoring aberrant hepatic circadian rhythm. Am. J. Physiol. Gastrointest. Liver Physiol. 2022;323(4):G387–400.

[48] Milagro FI, Gomez-Abellan P, Campion J, Martinez JA, Ordovas JM, Garaulet M. CLOCK, PER2 and BMAL1 DNA methylation: association with obesity and metabolic syndrome characteristics and monounsaturated fat intake. Chronobiol. Int. 2012;29(9):1180–94.

[49] Samblas M, Milagro FI, Mansego ML, Marti A, Martinez JA. PTPRS and PER3 methylation levels are associated with childhood obesity: results from a genome-wide methylation analysis. Pediatr. Obes. 2018;13(3):149–58.

[50] Sorkina O, Zaitseva O, Khudyakov A. The effect of long-term alcohol intoxication on the morphological structures and enzymatic activity of rat salivary glands. Alcohol 2022;99:23–33.

[51] Sacks FM, Andraski AB. Dietary fat and carbohydrate affect the metabolism of protein-based high-density lipoprotein subspecies. Curr. Opin. Lipidol. 2022;33(1):1–15.